

Giant Gating Tunability of Optical Refractive Index in Transition Metal Dichalcogenide Monolayers

Yiling Yu,^{†,‡} Yifei Yu,[†] Lujun Huang,[†] Haowei Peng,[§] Liwei Xiong,^{†,||} and Linyou Cao^{*,†,‡,||}

[†]Department of Materials Science and Engineering, [‡]Department of Physics, North Carolina State University, Raleigh, North Carolina 27695, United States

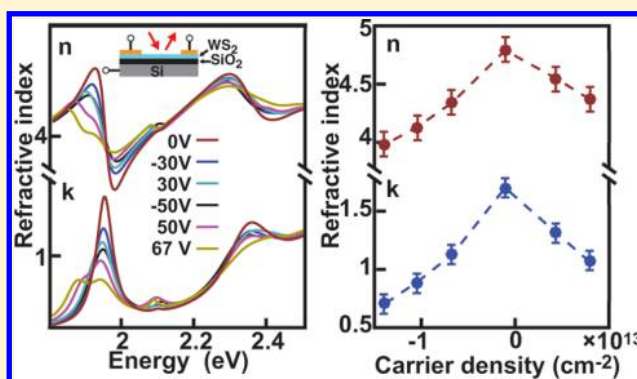
[§]Department of Chemistry, Temple University, Philadelphia, Pennsylvania 19405, United States

^{||}Hubei Key Laboratory of Plasma Chemistry and Advanced Materials, Wuhan Institute of Technology, Wuhan, 430205, P. R. China

Supporting Information

ABSTRACT: We report that the refractive index of transition metal dichalcogenide (TMDC) monolayers, such as MoS₂, WS₂, and WSe₂, can be substantially tuned by >60% in the imaginary part and >20% in the real part around exciton resonances using complementary metal–oxide–semiconductor (CMOS) compatible electrical gating. This giant tunability is rooted in the dominance of excitonic effects in the refractive index of the monolayers and the strong susceptibility of the excitons to the influence of injected charge carriers. The tunability mainly results from the effects of injected charge carriers to broaden the spectral width of excitonic interband transitions and to facilitate the interconversion of neutral and charged excitons. The other effects of the injected charge carriers, such as renormalizing bandgap and changing exciton binding energy, only play negligible roles. We also demonstrate that the atomically thin monolayers, when combined with photonic structures, can enable the efficiencies of optical absorption (reflection) tuned from 40% (60%) to 80% (20%) due to the giant tunability of the refractive index. This work may pave the way toward the development of field-effect photonics in which the optical functionality can be controlled with CMOS circuits.

KEYWORDS: 2D materials, transition metal dichalcogenide, photonics, electrical gating refractive index, exciton, WS₂



Electrically gating photons with complementary metal–oxide–semiconductor (CMOS) circuits has the potential to revolutionize the photonic industry. It would enable the development of unprecedented dynamic photonics with spatial and temporal resolutions comparable to that of state-of-art CMOS circuits. Of particular interest is the control of photons in the visible range as it would revolutionize the fields of imaging, cloaking, superlensing, and virtual reality. However, the electrical gating of photons is very challenging because of the difficulty in gating refractive index. Photons cannot be directly manipulated by electric fields because of charge neutrality and may only be controlled by virtue of light-matter interactions, including reflection, transmission, absorptions, and scattering. As refractive index stands as the most fundamental measure for light-matter interactions, to gate photons is in essence to gate refractive index. Numerous approaches have been reported to electrically tune refractive index, including plasma dispersion effect of free charges,^{1–6} electro-absorption effects (quantum confined stark effect⁷ and Keldysh effect^{5,8}), and nonlinear electro-optic effects such as Kerr⁹ or Pockels effects.¹⁰ But none of these approaches may provide satisfactory tuning efficiency, speed, spectral range, spatial resolution, and compatibility with CMOS circuits at the same time. For

instance, the optical absorption of injected charge carriers may give rise to changes in the refractive index, but the density of the charge carriers that can be injected using the conventional CMOS-gating is limited. This fundamentally limits the tunability in refractive index at the scale of 0.1–1%^{1,2,5,11} or the tuning spectrum at mid-IR or GHz, THz frequencies.^{3,4} While ionic gating has been recently reported able to inject higher densities of charges, which gives rise to larger tunability in visible frequencies,^{12–14} its nonlocal nature, inferior chemical stability, and intrinsically slow switching limits the operation speed, footprint, and compatibility with CMOS circuits. Additionally, electro-absorption effects, including Keldysh and quantum confined stark effects,^{7,8,15} have been reported able to induce change in optical absorption with the presence of electric fields in the vertical direction,^{7,8,15} but most of these works are in the infrared or even lower energy ranges, the tuning efficiency is often small (no more than few percent), or the structure is too bulky for integration with CMOS circuits.

Received: February 21, 2017

Revised: May 11, 2017

Published: May 15, 2017

Here we demonstrate that the refractive index of transition metal dichalcogenide (TMDC) monolayers, including MoS₂, WS₂, and WSe₂, can be substantially tuned by >60% in the imaginary part and >20% in the real part around excitonic resonance using CMOS-compatible electrical gating. This large tunability is achieved by leveraging on the strong excitonic effects of the monolayers¹⁶ and the high susceptibility of the excitons to the influence of free charge carriers. We further elucidate that the giant tunability in refractive index is mainly due to the effects of the injected charge carriers in broadening the spectral width of excitonic transitions and facilitating the interconversion of neutral and charged excitons. In contrast, the other effects of the injected charge carriers, such as renormalizing the bandgap and changing the exciton binding energy, play only negligible roles. It is worthwhile to point out that, although many previous studies have reported electrical tunability in the light absorption and emission of TMDC monolayers,^{17–22} this work is the first ever quantitatively demonstrating the tunability in refractive index and unambiguously elucidating the underlying physics. Additionally, we use a simple design to illustrate that, when combined with optical resonant structures, the tunability of refractive index in the atomically thin monolayers may enable substantial change in light reflection and absorption.

We start with examining the spectral reflectance (the intensity ratio of the light reflected from the monolayer and the light reflected from a mirror) of TMDC monolayers under electrical gating. Figure 1a inset schematically illustrates the

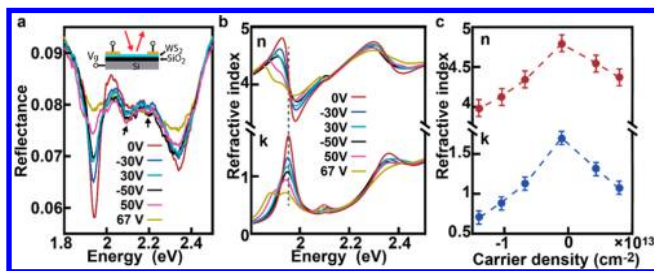


Figure 1. Gated reflection and refractive index of monolayer WS₂. (a) Reflection spectra of monolayer WS₂ at different gating voltages. The inset is a schematic illustration for the measurement configuration. The two arrows point out the two excited states of the A exciton, 2S and 3S. (b) Fitted real part n and imaginary part k of the refractive index with different gating voltages. (c) The peak value of the real part (at around 1.92 eV) and the imaginary part (at around 1.95 eV) as a function of carrier densities.

measurement configuration. The monolayers (obtained from a 2D layer) are grown on degenerately doped Si substrates with thermally grown silicon oxide (SiO₂/Si) using chemical vapor deposition (CVD) processes. The source and drain electrodes (5 nm Ti/50 nm Au) are fabricated on top of the monolayer using standard e-beam lithography and metallization procedures. We have confirmed that the electrodes form Ohmic contact with the monolayers (Figure S5b inset). In experiments, the Si substrate is used as the gate, and identical potentials are applied to the source and drain electrodes. Figure 1a shows the spectral reflection collected from monolayer WS₂ under different gating voltages. The reflection of the A exciton (~1.95 eV) shows substantial variation with the gating voltage, but the B (~2.35 eV) and C excitons (~2.70 eV, Figure S1) show much less or even negligible variation. The appearance of the gated variation only at the excitonic peaks suggests that this

is not caused by the plasma dispersion effect of free charge carriers, which would give rise to changes over a broad spectral range. Similar gating tunability in reflectance can also be observed at monolayer MoS₂ and WSe₂ (Figure S2). The larger tunability in magnitude for WS₂ likely stems from its larger excitonic absorption compared to MoS₂ and WSe₂.²³

We can obtain refractive index from the measured spectral reflection using a Kramers–Kronig constrained analysis. Basically, we fit the complex dielectric function $\epsilon = \epsilon_1 + i\epsilon_2$ of the monolayer as a sum of contribution from multiple Lorentz oscillators:^{24,25}

$$\epsilon(E) = \epsilon_\infty + \sum_j \frac{f_j}{E_j^2 - E^2 - iE\gamma_j} \quad (1)$$

where ϵ_∞ is the high-frequency dielectric constant and E_j and γ_j are the resonant energy and damping factor of the j th oscillator, respectively. f_j is a phenomenal parameter involving contribution from transition matrix element, density of states, and excitonic effects. Additionally, we fit the reflection of the monolayer on the top of SiO₂/Si substrates using a model for the reflection of multilayer structures as²⁶

$$R = |r|^2 = \left| \frac{\rho_1 + \rho_1 e^{-i2k_1 d_1} + \rho_1 \rho_2 \rho_3 e^{-i2k_2 d_2} + \rho_3 e^{-i2(k_1 d_1 + k_2 d_2)}}{1 + \rho_2 \rho_1 e^{-i2k_1 d_1} + \rho_2 \rho_3 e^{-i2k_2 d_2} + \rho_1 \rho_3 e^{-i2(k_1 d_1 + k_2 d_2)}} \right|^2 \quad (2)$$

where $\rho_1 = (n_1 - n_0)/(n_1 + n_0)$, $\rho_2 = (n_2 - n_1)/(n_1 + n_2)$, and $\rho_3 = (n_3 - n_2)/(n_2 + n_3)$. n_0 , n_1 , n_2 , and n_3 are the refractive index of air, the monolayer, SiO₂, and Si, respectively. k_1 and k_2 are the wavenumbers in the monolayer and SiO₂ as $k_1 = n_1 2\pi/\lambda$ and $k_2 = n_2 2\pi/\lambda$. d_1 and d_2 are the thickness of the monolayer and the SiO₂. The refractive index of the monolayer n_2 can be correlated to the fitted dielectric function ϵ as $n_2^2 = \epsilon$. To get accurate determination of the dielectric function ϵ , the Kramers–Kronig constrained analysis requires information in the full spectral range, but the measured spectral reflection only cover the range of 1.8–2.5 eV. To address this issue, we ignore the contribution from the oscillators in lower energy ranges as it is expected to be weak for the refractive index in the visible range. However, the contribution from the oscillators at higher energy ranges has to be considered. We assume that the dielectric function of the monolayer at the higher energy ranges is similar to that of bulk counterparts and use the dielectric function of the bulk counterparts, which is available in ref 27, to correct the oscillators of the monolayers in the higher energy range. This strategy has been previously demonstrated able to give rise to reasonably accurate dielectric function of TMD monolayers from spectral reflectance.²³ We have also confirmed that the refractive index obtained using this strategy is indeed consistent with what measured from spectral ellipometry, the standard characterization techniques for dielectric functions (Figure S8). More detailed description about the fitting process can be found at the Supporting Information. Three major oscillators are involved in the measured spectral reflection, including the neutral A exciton (A_0), the charged A trion (A_- or A_+), and the B exciton. The resonant energy E_j and damping factor γ_j for each of the oscillators can be found out from the measured spectral reflection (Figure 1a). There are another two small oscillators corresponding to the excited states (2S and

3S) of the A exciton as indicated by the black arrows in Figure 1a,²⁸ but they can be ignored due to trivial contribution.

Figure 1b shows the refractive index obtained from the analysis. The fitted reflection spectra match the experimental results very well (Figure S3). Additionally, the sum rule holds for the fitted reflective index under all the different gating voltages²⁹ as the integration of the fitted absorption coefficient $\alpha(\omega)$ over the full spectrum range (up to 6 eV) always gives rise to similar values regardless the gating voltage (Figure S4). All of these further support the validity of the fitting method. The refractive index at the frequencies around the A exciton shows substantial tunability, the real part tuned from 4.80 to 3.97 and the imaginary part from 1.7 to 0.7 when the gating voltage V_g is changed from 0 to 67 V. This is 2 orders of magnitude higher than what previously reported for tuning the refractive index in the visible range by electrical gating.¹¹ Note that the maximal tunability of the real and imaginary parts appears at different frequencies, 1.95 eV for the imaginary part and around 1.92 eV for the real part. This is rooted in the conjugation nature of the real and imaginary parts of dielectric functions. To further illustrate the tunability, we plot the real part of the refractive index at 1.92 eV and the imaginary part at 1.95 eV as a function of the density of charge carriers in Figure 1c. The charge density is estimated using the capacitor model $Q = C_{ox}(V_g - V_{th})$, in which C_{ox} is the oxide capacitance, V_g is the gate voltage, and V_{th} is the threshold voltage for charge neutrality in the monolayer that we find to be around -7 V from PL¹⁸ and $I-V$ measurements (Figure S5). Both the real and the imaginary parts of the refractive index show a maximum at the point of charge neutrality and decrease with the density of charge carriers (either electrons or holes) increasing.

The observed tunability in refractive index can be mainly correlated to the gated variation in the absorption of the neutral A exciton (A_0). This is evidenced by the imaginary part of the dielectric function ϵ_2 (Figure S6), which is known proportional to optical absorption and may uniquely determine the real part of the dielectric function via the Kramers–Kronig relationship.²⁵ The fitting result for ϵ_2 indicates that only the absorption of the neutral A exciton (A_0) shows substantial variation with electrical gating. For the convenience of discussion, we only focus on the on-resonance absorption of A_0 that is proportional to $\epsilon_2 = f_{A_0}/(E_{A_0}\gamma_{A_0})$. The resonant frequency E_{A_0} does not change much with the gating voltage (Figure 2a). Therefore, the observed tunability in refractive index is essentially dictated by the variation of f_{A_0} and γ_{A_0} under electrical gating. To better illustrate this notion, we plot γ_{A_0} (obtained from Figure 1a) and f_{A_0} (obtained from the Kramers–Kronig constrained analysis with eq 1) as a function of charge carrier densities in Figure 2b–c. The f and γ of the charged A exciton (A_{\pm}) are also plotted in Figure 2 as reference.

We may better understand the physics underlying the gated variation of f_{A_0} and γ_{A_0} through analysis for the effect of the injected charge carriers. Generally, the injected charge carriers may affect the optical properties of low-dimensional semiconductor materials through three major physical mechanisms: Pauli blocking, Coulomb scattering, and dielectric screening. The Pauli blocking causes phase space filling up to Fermi level (Table S1), which will lead to a blue shift of the optical gap energy. The Coulomb scattering, through which excitons interact with the injected charge carriers, may broaden the spectral width of excitonic absorption by enhancing the dephasing rate and also facilitate the formation of charged

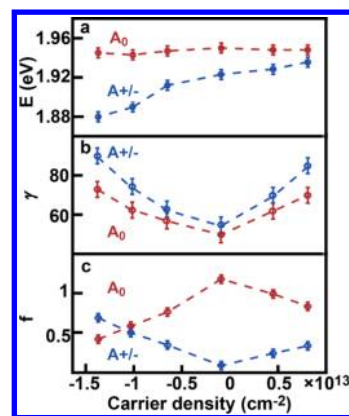


Figure 2. Gating tunability of physical parameters in monolayer WS₂. (a) Optical bandgap E (b) damping factor γ , and (c) f that representing the oscillation strength of the neutral (A_0) and charged (A_{\pm}) excitons. The error bar given in the figure represents the error in fitting the measured spectral reflectance.

excitons. The screening of Coulomb interactions may lead to bandgap renormalization and change in the exciton binding energy.^{28,30,31} The bandgap renormalization and the change in exciton binding energy can be estimated from Raman measurements. The intensity ratio of the two characteristic Raman peaks of monolayer WS₂, $E_{2g}/2LA(M)$, and A_{1g} decreases with the charge carrier density increasing (Figure 3a). This can be correlated to the bandgap renormalization as

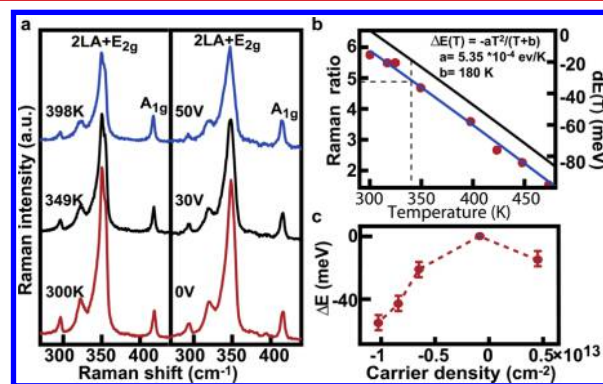


Figure 3. Bandgap renormalization and change in exciton binding energy in monolayer WS₂. (a) Comparison of Raman spectra of monolayer WS₂ at different temperatures (left) and different gating voltages (right). The intensity is normalized to that of the A_{1g} peak. (b) The measured (red dots) and fitted (blue line) Raman intensity ratio as a function of the temperature (red dots). The black curve is the calculated bandgap shift of the monolayer as a function of temperature, in which the bandgap at 300 K is used as the reference. The dashed lines indicate one Raman intensity ratio measured at the monolayer under electrical gating. (c) The estimated bandgap renormalization of monolayer WS₂ as a function of the density of charge carriers.

the intensity of the $E_{2g}/2LA(M)$ peak is related with the band structure due to the involvement of double resonances.³² We can estimate the amplitude of the bandgap renormalization by comparing the Raman spectra measured at different gating voltages to those collected under different temperatures. This is because the Raman intensity ratio decreases with the temperature increasing, and the temperature dependence is similar to the dependence of the intensity ratio on the gating voltage (Figure 3a). Briefly, we identify the temperature under

which the Raman intensity ratio is comparable to what observed at specific gating voltages and then estimate the bandgap renormalization based on a well-established temperature-bandgap correlation (Figure 3b).³³ For simplicity, the effect of temperatures on the exciton binding energy is ignored, which is reasonable given the relative small temperature change in our experiments (300–450 K). The estimated bandgap renormalization ΔE_g (using the bandgap at the gating voltage of 0 V as reference) is plotted as a function of the density of charge carriers in Figure 3c. With the information on bandgap renormalization ΔE_g , we can derive the change in exciton binding energy ΔE_{ex} from the change in the optical bandgap ΔE_{opt} as $\Delta E_{opt} = \Delta E_g - \Delta E_{ex} + \Delta E_F$. E_F here is the Fermi energy that indicates the phase space filling effect. For the neutral A exciton, ΔE_{ex} is smaller than 30 meV in our gated voltage range (ΔE_F and ΔE_g can be obtained from Table S1, Figure 2a). By the same token, we may also estimate ΔE_{ex} of the charged A exciton (see Table S1).

It is obvious that the Coulomb scattering is the major mechanism for the gated variation in the damping factor γ . We can find out the mechanism governing the gated variation of f through fitting the dielectric function with a model of Wannier excitons in fractional dimension space. The fractional dimensional space model has previously been established to describe the optical properties of quantum wells.^{34–39} It treats highly anisotropic excitons in low-dimensional structures to be isotropic in a fractional-dimensional space and defines an effective dimensionality d based on the excitonic binding energies in bulk materials R and the low-dimensional structure E_{ex} as $d = 1 + 2(R/E_{ex})^{0.5}$. One major advantage of the fractional dimension space model lies in its capability to quantitatively evaluate the contribution of excitonic effect, which is realized by introducing the effective dimensionality to the calculation of joint density of states. According to the fractional dimension space model, the complex dielectric function ϵ_j at an arbitrary energy E contributed by one excitonic transition can be written as $\epsilon_j = S_j \cdot G_j$, where S_j is a parameter representing the transition probability and G_j is an effective joint density of state in which the excitonic effect is represented by the effective dimensionality d .^{34–39} More specifically,

$$S_j = F |p_{vc}|^2 \quad (3)$$

$$G_j = \frac{R^{d/2-1}}{(E + i\gamma_j)^2} [g_d(\xi(E + i\gamma_j)) + g_d(\xi(-E - i\gamma_j)) - g_d(\xi(0))]$$

$$g_d(\xi) = \frac{2\pi\Gamma((d-1)/2 + \xi)}{\Gamma((d-1)/2)^2\Gamma(1 - (d-1)/2 + \xi)\xi^{d-2}} \times [\cot \pi((d-1)/2 - \xi) - \cot \pi(d-1)]$$

where F is a constant prefactor, p_{vc} is the matrix element for the interband transition, μ is the reduced effective mass of electrons, e and m_0 are the charge and mass of free electrons, ϵ_0 and \hbar are the vacuum permittivity and the Planck's constant, Γ is the gamma function, and ξ is a function related with the electronic bandgap E_g and R as $\xi(z) = [R/(E_g - z)]^2$. The exciton binding energy in monolayer and bulk WS_2 is set to be 0.7 eV^{40,41} and 0.055 eV,²⁷ respectively. The other parameters, including the effective dimensionality d , electronic bandgap E_g , and damping factor γ , can be obtained from either the known

binding energy, the experimental measurement, or the preceding discussion. We use eq 3 to fit the dielectric function. Basically, we first calculate G_j using the known parameters and then fit the value of S_j to match the measured reflection spectra (Figure S7).

The fitting result indicates that the gated variation in f_{A0} mainly results from the interconversion of neutral and charged A excitons. Figure 4a shows the fitted S_j for the neutral (A_0)

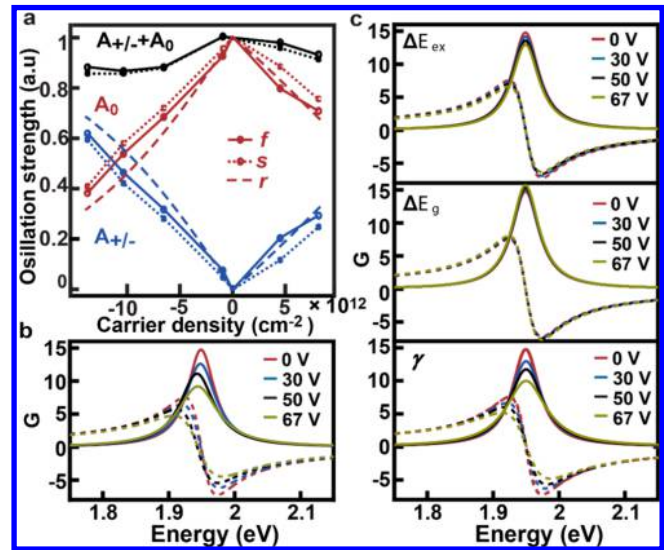


Figure 4. Dominating mechanism for the tunable refractive index. (a) Fitting results for S and f of the neutral and charged A excitons as a function of charge carrier densities. The black solid and dashed lines indicate the sum of the values for both neutral and charged excitons. The calculated fractions of the neutral and charged excitons r are also given. (b) Calculated G of the neutral A exciton with different gating voltages. (c) Calculated G of the neutral A exciton as a function of (upper) change in exciton binding energy, (middle) bandgap renormalization, and (lower) change in the damping factor γ . The spectra in the upper and middle panels are artificially shifted to align the peak position for the convenience of comparison.

and charged (A_{\pm}) excitons at different carrier densities. We can get useful physical insight by comparing S_j to f_j as shown in Figure 4a. For the convenience of comparison, all of the results are normalized to the sum of the values for both neutral and charged excitons ($S_{A0} + S_{A_{\pm}}$ and $f_{A0} + f_{A_{\pm}}$) at each gating voltages, respectively. The S_j and f_j show very similar dependence on the charge carrier density. This indicates that the enhancement by excitonic effects to the oscillation strength, which is involved in f_j but not in S_j , does not change much with the gating voltage. The variation in f_j under electrical gating mainly results from change in the transition matrix element p_{vc} instead of a change in the excitonic effect. Additionally, the sum of the S_j for the neutral and charged excitons together remains to be reasonably constant regardless the gating voltage. This suggests that the interband transitions of the neutral and charged excitons are competing processes that involve the same ground state. The change of the S_j for the neutral and charged excitons with gating voltages results from the interconversion between the neutral and the charged excitons, which is indicated by the redistribution of the transition matrix element p_{vc} among the neutral and the charged excitons.

The correlation of gated variation in f_j to the interconversion of neutral and charged excitons may be further supported by the thermal equilibrium distribution of the excitons. We use the

negatively charged exciton as an example to illustrate this notion. The interconversion of the neutral and negatively charged exciton can be written as $A_0 + e \leftrightarrow A_-$. Following what has been previously studied,^{42,43} we assume that, in the temperature and photoexcitation range of our experiments, the monolayer consisting of the neutral and charged excitons behaves as a two-level system in equilibrium. The thermal equilibrium distribution of the neutral and charged excitons is dictated by the chemical potential of the injected electrons ξ and the binding energy of the charged exciton E_b^{A-} . The chemical potential of a two-dimensional ideal Fermion gas can be written as $\xi = k_B T \ln(e^{E_F/k_B T} - 1)$, where k_B and T are the Boltzmann constant and temperature, respectively. E_F is the Fermi energy of the injected electrons at the conduction band and can be calculated with $E_F = \pi \hbar^2 n_e / (2m_e)$, where n_e and m_e are the density and effective mass of the injected electrons, and the constant 2 stands for valley degeneracy of the monolayer.⁴⁴ The ratio between the densities of the neutral (n_{A_0}) and charged (n_{A_-}) excitons under thermal equilibrium is a function of the binding energy of charged exciton $\frac{n_{A_0}}{n_{A_-}} = 4e^{(-E_b^{A-} - \xi)/k_B T}$, where the factor 4 is the degeneracy ratio of the neutral and charged excitons.⁴² Therefore, the fractions of the neutral and charge excitons are defined as $r_{A_0} = n_{A_0}/(n_{A_0} + n_{A_-})$ and $r_{A_-} = n_{A_-}/(n_{A_0} + n_{A_-})$. We can estimate the binding energy E_b^{A-} from the measured optical bandgaps of the neutral (E_{A_0}) and charge (E_{A_-}) excitons and the binding energy as $E_b^{A-} = E_{A_0} - E_{A_-} - E_F$. A similar analysis can be performed for the positively charged A exciton (A_+). With all of the information, we can calculate the fractions r_{A_0} and r_{A_-} as a function of the density of injected charge carriers (see Table S1 in the Supporting Information for the parameters used in the calculation). The calculation results are plotted in Figure 4a. It shows reasonable consistency with the f_j , further indicating the gated variation of f_j can be mainly ascribed to the interconversion of the neutral and charged excitons.

The fitting result confirms that the damping factor γ is important for the observed tunability in refractive index. It also indicates that the change in excitonic binding energy ΔE_{ex} and the bandgap renormalization ΔE_g play negligible roles. These variables are all included in the parameter G_j , but not S_j . We examine G_j as a function of each of the variable. The change in the damping factor γ dominates the variation in G_j , while the change in binding energy ΔE_{ex} (represented by change in the effective dimensionality d) and the bandgap renormalization ΔE_g (represented by change in the electronic bandgap E_g) may only have minor effects (Figure 4c). Intuitively, this result is understandable as the ΔE_{ex} and ΔE_g are more than 1 order of magnitude smaller than the exciton binding energy and bandgap, respectively.

As the intrinsic optical response of 2D TMDC materials is weak due to the atomically thin dimension, the development of field-effect photonic devices for practical applications would require substantial enhancement in the optical response, and this can be achieved by leveraging on the power of optical resonance.⁴⁵ To illustrate this notion, we have designed a GaN based grating structure on Al_2O_3 with monolayer WS_2 covered on the top and a silver mirror at the bottom as illustrated in Figure 5a. The GaN layer is heavily doped serve as back gate with a thin layer HfO_2 on top as insulating gate dielectric layer. The top electrode Ti/Au is directly deposit on top of the monolayer WS_2 . The thickness of monolayer WS_2 is 0.62 nm. Our calculation indicates that the absorption and reflectance

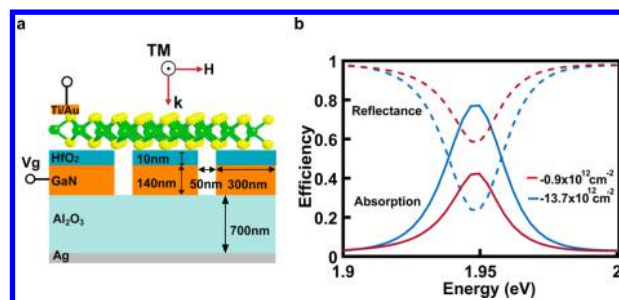


Figure 5. Gating optical functionality. (a) Illustration of configuration of the photonic device. (b) Simulated absorption efficiency (solid line) and reflectance (dashed line) correspond to different electron injections induced by gate voltages.

can be electrically tuned in the range of 40–80% when the charge carrier is tuned from $-0.9 \times 10^{12} \text{ cm}^{-2}$ to $-13.7 \times 10^{12} \text{ cm}^{-2}$. The details of the design principle can be found in the Supporting Information (S2).

In conclusion, we have demonstrated giant gating tunability in the refractive index (>60% in the imaginary part and >20% in the real part) around exciton resonances of atomically thin TMDC monolayers. We believe that even larger tunability can be achieved with optimization in the device fabrication. Additionally, we have elucidated that the tunability mainly results from the spectral broadening (γ) and the interconversion of the neutral and charged excitons caused by the injected charge carriers. In contrast, the other effects of the injected charge carriers, including bandgap renormalization and change in exciton binding energy, only play negligible roles. The result provides new insight into the fundamental optical properties of 2D TMDC materials. For instance, changing the substrate and dielectric environment of 2D TMDC materials, which is expected to change the screening of Coulomb interactions, may not affect the dielectric function of 2D TMDC materials much¹⁶ unless the changing may induce substantial change in the exciton spectral width or the doping to the materials.⁴⁶ More importantly, this result may open up a new age of field-effect photonics whose optical functionality can be electrically controlled in ways similar to that of state-of-art CMOS circuits. We also demonstrate by combining with the nanophotonic structure, the weak absorption nature of 2D TMDC could be overcome and lead to 40% absorption/reflection modulation.

■ ASSOCIATED CONTENT

📄 Supporting Information

The Supporting Information is available free of charge on the ACS Publications website at DOI: 10.1021/acs.nanolett.7b00768.

Experimental Methods, supporting figures and supporting table (PDF)

■ AUTHOR INFORMATION

Corresponding Author

*E-mail: lcao2@ncsu.edu.

ORCID

Linyou Cao: 0000-0002-7834-8336

Notes

The authors declare no competing financial interest.

ACKNOWLEDGMENTS

This work was supported by the National Science Foundation under the grant ECCS-1508856. The theoretical analysis and discussion are supported as part of the Center for the Computational Design of Functional Layered Materials, an Energy Frontier Research Center funded by the U.S. Department of Energy, Office of Science, Basic Energy Sciences under Grant No. DE-SC0012575. The authors acknowledge the use of the Analytical Instrumentation Facility (AIF) at North Carolina State University, which is supported by the State of North Carolina and the National Science Foundation.

REFERENCES

- (1) Bennett, B. R.; Soref, R. A.; Del Alamo, J. A. D. *IEEE J. Quantum Electron.* **1990**, *26*, 113.
- (2) Xu, F.; Das, S.; Gong, Y.; Liu, Q.; Chien, H.-C.; Chiu, H.-Y.; Wu, J.; Hui, R. *Appl. Phys. Lett.* **2015**, *106*, 031109.
- (3) Liu, M.; Yin, X. B.; Ulin-Avila, E.; Geng, B. S.; Zentgraf, T.; Ju, L.; Wang, F.; Zhang, X. *Nature* **2011**, *474*, 64–67.
- (4) Ju, L.; Geng, B. S.; Horng, J.; Girit, C.; Martin, M.; Hao, Z.; Bechtel, H. A.; Liang, X. G.; Zettl, A.; Shen, Y. R.; Wang, F. *Nat. Nanotechnol.* **2011**, *6*, 630–634.
- (5) Soref, R.; Bennett, B. *IEEE J. Quantum Electron.* **1987**, *23*, 123–129.
- (6) Xu, Q.; Schmidt, B.; Pradhan, S.; Lipson, M. *Nature* **2005**, *435*, 325–327.
- (7) Kuo, Y.-H.; Lee, Y. K.; Ge, Y.; Ren, S.; Roth, J. E.; Kamins, T. I.; Miller, D. A. B.; Harris, J. S. *Nature* **2005**, *437*, 1334–1336.
- (8) Seraphin, B. O.; Bottka, N. *Phys. Rev.* **1965**, *139*, A560–A565.
- (9) Lettieri, S.; Maddalena, P. *J. Appl. Phys.* **2002**, *91*, 5564–5570.
- (10) Liu, A. S.; Liao, L.; Rubin, D.; Nguyen, H.; Ciftcioglu, B.; Chetrit, Y.; Izhaky, N.; Paniccia, M. *Opt. Express* **2007**, *15*, 660–668.
- (11) Reed, G. T.; Mashanovich, G.; Gardes, F. Y.; Thomson, D. J. *Nat. Photonics* **2010**, *4*, 660.
- (12) Lee, E. J.; Choi, S. Y.; Jeong, H.; Park, N. H.; Yim, W.; Kim, M. H.; Park, J. K.; Son, S.; Bae, S.; Kim, S. J.; Lee, K.; Ahn, Y. H.; Ahn, K. J.; Hong, B. H.; Park, J. Y.; Rotermund, F.; Yeom, D. I. *Nat. Commun.* **2015**, *6*, 6851.
- (13) Liu, Y.; Tom, K.; Wang, X.; Huang, C.; Yuan, H.; Ding, H.; Ko, C.; Suh, J.; Pan, L.; Persson, K. A.; Yao, J. *Nano Lett.* **2016**, *16*, 488–496.
- (14) Thareja, V.; Kang, J. H.; Yuan, H. T.; Milaninia, K. M.; Hwang, H. Y.; Cui, Y.; Kik, P. G.; Brongersma, M. L. *Nano Lett.* **2015**, *15*, 1570–1576.
- (15) Klein, J.; Wierzbowski, J.; Regler, A.; Becker, J.; Heimbach, F.; Müller, K.; Kaniber, M.; Finley, J. J. *Nano Lett.* **2016**, *16*, 1554–1559.
- (16) Yu, Y.; Yu, Y.; Cai, Y.; Li, W.; Gurarlan, A.; Peelaers, H.; Aspnes, D. E.; Van de Walle, C. G.; Nguyen, N. V.; Zhang, Y.-W.; Cao, L. *Sci. Rep.* **2015**, *5*, 16996.
- (17) Chernikov, A.; van der Zande, A. M.; Hill, H. M.; Rigosi, A. F.; Velauthapillai, A.; Hone, J.; Heinz, T. F. *Phys. Rev. Lett.* **2015**, *115*, 126802.
- (18) Ross, J. S.; Wu, S.; Yu, H.; Ghimire, N. J.; Jones, A. M.; Aivazian, G.; Yan, J.; Mandrus, D. G.; Xiao, D.; Yao, W.; Xu, X. *Nat. Commun.* **2013**, *4*, 1474.
- (19) Mak, K. F.; He, K.; Lee, C.; Lee, G. H.; Hone, J.; Heinz, T. F.; Shan, J. *Nat. Mater.* **2012**, *12*, 207.
- (20) Newaz, A. K. M.; Prasai, D.; Ziegler, J. I.; Caudel, D.; Robinson, S.; Haglund, R. F.; Bolotin, K. I. *Solid State Commun.* **2013**, *155*, 49–52.
- (21) Liu, Q. H.; Li, L. Z.; Li, Y. F.; Gao, Z. X.; Chen, Z. F.; Lu, J. J. *Phys. Chem. C* **2012**, *116*, 21556–21562.
- (22) Liu, B.; Zhao, W.; Ding, Z.; Verzhbitskiy, I.; Li, L.; Lu, J.; Chen, J.; Eda, G.; Loh, K. P. *Adv. Mater.* **2016**, *28*, 6457–6464.
- (23) Li, Y.; Chernikov, A.; Zhang, X.; Rigosi, A.; Hill, H. M.; van der Zande, A. M.; Chenet, D. A.; Shih, E.-M.; Hone, J.; Heinz, T. F. *Phys. Rev. B: Condens. Matter Mater. Phys.* **2014**, *90*, 205422.
- (24) Wooten, F. *Optical properties of solids*; Academic Press: New York and London, 1972.
- (25) Chuang, S. L. *Physics of Optoelectronic Devices*; John Wiley & Sons: New York, 1995.
- (26) Orfanidis, S. J. *Electromagnetic Waves and Antennas*; Rutgers University Press: Piscataway, NJ, 2008.
- (27) Beal, A. R.; Liang, W. Y.; Hughes, H. P. *J. Phys. C: Solid State Phys.* **1976**, *9*, 2449.
- (28) Chernikov, A.; Berkelbach, T. C.; Hill, H. M.; Rigosi, A.; Li, Y.; Aslan, O. B.; Reichman, D. R.; Hybertsen, M. S.; Heinz, T. F. *Phys. Rev. Lett.* **2014**, *113*, 076802.
- (29) Gordon, R. G. *J. Chem. Phys.* **1963**, *38*, 1724–1729.
- (30) Tarucha, S.; Kobayashi, H.; Horikoshi, Y.; Okamoto, H. *Jpn. J. Appl. Phys.* **1984**, *23*, 874.
- (31) Ugeda, M. M.; Bradley, A. J.; Shi, S. F.; da Jornada, F. H.; Zhang, Y.; Qiu, D. Y.; Ruan, W.; Mo, S. K.; Hussain, Z.; Shen, Z. X.; Wang, F.; Louie, S. G.; Crommie, M. F. *Nat. Mater.* **2014**, *13*, 1091–1095.
- (32) Berkdemir, A.; Gutiérrez, H. R.; Botello-Méndez, A. R.; Perea-López, N.; Elías, A. L.; Chia, C.-I.; Wang, B.; Crespi, V. H.; López-Urías, F.; Charlier, J.-C.; Terrones, H.; Terrones, M. *Sci. Rep.* **2013**, *3*, 1755.
- (33) Gaur, A. P. S.; Sahoo, S.; Scott, J. F.; Katiyar, R. S. *J. Phys. Chem. C* **2015**, *119* (9), 5146–5151.
- (34) He, X.-F. *Phys. Rev. B: Condens. Matter Mater. Phys.* **1990**, *42*, 11751–11756.
- (35) Tanguy, C. *Phys. Rev. Lett.* **1995**, *75*, 4090–4093.
- (36) Tanguy, C.; Lefebvre, P.; Mathieu, H.; Elliott, R. J. *J. Appl. Phys.* **1997**, *82*, 798–802.
- (37) Marquezini, M. V.; Tignon, J.; Hasche, T.; Chemla, D. S. *Appl. Phys. Lett.* **1998**, *73*, 2313–2315.
- (38) Lefebvre, P.; Christol, P.; Mathieu, H. *Phys. Rev. B: Condens. Matter Mater. Phys.* **1993**, *48*, 17308–17315.
- (39) Lefebvre, P.; Christol, P.; Mathieu, H.; Glutsch, S. *Phys. Rev. B: Condens. Matter Mater. Phys.* **1995**, *52*, 5756–5759.
- (40) Ye, Z.; Cao, T.; O'Brien, K.; Zhu, H.; Yin, X.; Wang, Y.; Louie, S. G.; Zhang, X. *Nature* **2014**, *513*, 214–218.
- (41) Zhu, B.; Chen, X.; Cui, X. Exciton Binding Energy of Monolayer WS₂. *Sci. Rep.* **2015**, *5*, 9218.
- (42) Manassen, A.; Cohen, E.; Ron, A.; Linder, E.; Pfeiffer, L. N. *Phys. Rev. B: Condens. Matter Mater. Phys.* **1996**, *54*, 10609.
- (43) Ron, A.; Yoon, H. W.; Sturge, M. D.; Manassen, A.; Cohen, E.; Pfeiffer, L. N. *Solid State Commun.* **1996**, *97*, 741–745.
- (44) Ovchinnikov, D.; Allain, A.; Huang, Y. S.; Dumcenco, D.; Kis, A. *ACS Nano* **2014**, *8*, 8174–8181.
- (45) Huang, L. J.; Li, G. Q.; Gurarlan, A.; Yu, Y. L.; Kirste, R.; Guo, W.; Zhao, J. J.; Collazo, R.; Sitar, Z.; Parsons, G. N.; Kudenov, M.; Cao, L. Y. *ACS Nano* **2016**, *10*, 7493–7499.
- (46) Yu, Y.; Yu, Y.; Xu, C.; Cai, Y.-Q.; Su, L.; Zhang, Y.; Zhang, Y.-W.; Gundogdu, K.; Cao, L. *Adv. Funct. Mater.* **2016**, *26*, 4733–4739.